2D Dark-Count-Rate Modeling of PureB Single-Photon Avalanche Diodes in a TCAD Environment

Tihomir Knežević*[a], Lis K. Nanver[b], Tomislav Suligoj[a]
[a]University of Zagreb, Faculty of Electrical Engineering and Computing, Micro and Nano Electronics Laboratory, Croatia; [b]University of Twente, Faculty of Electrical Engineering Mathematics & Computer Science, Enschede, The Netherlands

ABSTRACT

PureB silicon photodiodes have nm-shallow p^+n junctions with which photons/electrons with penetration-depths of a few nanometer can be detected. PureB Single-Photon Avalanche Diodes (SPADs) were fabricated and analysed by 2D numerical modeling as an extension to TCAD software. The very shallow p^+-anode has high perimeter curvature that enhances the electric field. In SPADs, noise is quantified by the dark count rate (DCR) that is a measure for the number of false counts triggered by unwanted processes in the non-illuminated device. Just like for desired events, the probability a dark count increases with increasing electric field and the perimeter conditions are critical. In this work, the DCR was studied by two 2D methods of analysis: the "quasi-2D" (Q-2D) method where vertical 1D cross-sections were assumed for calculating the electron/hole avalanche-probabilities, and the "ionization-integral 2D" (II-2D) method where cross-sections were placed where the maximum ionization-integrals were calculated. The Q-2D method gave satisfactory results in structures where the peripheral regions had a small contribution to the DCR, such as in devices with conventional deep-junction guard rings (GRs). Otherwise, the II-2D method proved to be much more precise. The results show that the DCR simulation methods are useful for optimizing the compromise between fill-factor and p-/n-doping profile design in SPAD devices. For the experimentally investigated PureB SPADs, excellent agreement of the measured and simulated DCR was achieved. This shows that although an implicit GR is attractively compact, the very shallow pn-junction gives a risk of having such a low breakdown voltage at the perimeter that the DCR of the device may be negatively impacted.

Keywords: photodiode, single-photon avalanche diodes (SPADs), detectors, silicon, pure boron, guard rings

1. INTRODUCTION

High sensitivity in low-light conditions is readily achieved by using avalanche photodiodes (APDs). APDs operated in Geiger mode, reversely biased above breakdown voltage (V_{BR}), have infinite internal gain allowing detection of a single photon. These APDs are usually called single-photon avalanche detectors (SPADs). Single-photon detection is utilized in a number of different fields such as deep space communication[1], 3D imaging[2,3], medical and biological imaging[4–6], laser optical ranging (LIDAR/LADAR) systems[3] and quantum communication applications[7] - in particular quantum key distribution[8,9]. Fields such as medical imaging, advanced lithography and electron microscope imaging can profit from the use of very low-penetration-depth beams that may include near-, vacuum- and extreme-ultraviolet light and low-energy electrons (100 – 1000 eV). The photosensitive region in Si must then extend to within a few nm of the light-entrance window surface to obtain high responsivity. Other desired properties are low noise, high stability during exposure, robustness with respect to the sometimes-harsh detection environment, and, most importantly, compatibility with CMOS for integration of the read-out circuitry. PureB photodiodes have met these requirements[10–12] and are in production as regular photodiodes while research into SPAD integration is on-going[13,14].

In SPADs which are operated at an excess bias voltage of $V_{EX} = V_D - V_{BR}$, a self-sustained avalanche can be triggered by the photo-generated carriers. The photon detection efficiency (PDE) is the ratio of the number of the photons detected by the SPAD and the number of incident photons. The PDE gives a measure of the sensitivity of the SPAD to the impinging radiation. Other than the incoming photons, the avalanche can be started by unwanted processes such as thermally generated carriers and carriers generated due to tunneling or background photons[15,16]. This noise of the device is characterized by the dark count rate (DCR). Thermal carrier generation is dominated by the Shockley-Read-Hall (SRH) process. Carrier generation due to tunneling can be attributed to band-to-band tunneling (BTBT) or trap-assisted tunneling (TAT). Both mechanisms depend on the magnitude of the electric field in the semiconductor leading to an exponential increase of the DCR with V_{EX}[17]. Moreover, counts can be triggered by the release of carriers from deep energy levels. This

*tihomir.knezevic@fer.hr; phone 385 1 6129-564; minel.fer.hr

Physics and Simulation of Optoelectronic Devices XXVI, edited by Bernd Witzigmann, Marek Osiński, Yasuhiko Arakawa, Proc. of SPIE Vol. 10526, 105261K · © 2018 SPIE
CCC code: 0277-786X/18/$18 · doi: 10.1117/12.2290757

is a secondary effect attributed to the operation of the SPAD called afterpulsing. Deep levels are filled during the avalanche process and the spontaneous release of deep-level carriers can trigger additional counts[18,19].

Simulations of the DCR and PDE are not directly available in commercially available TCAD software such as Sentaurus Device[20]. A TCAD-based simulation environment capable of simulating the DCR and PDE characteristics of SPADs is developed by the authors based on avalanche probability calculations in 1D[21]. The simulation procedure is adopted from[22] but with the main advantage of using TCAD in the simulations. However, to properly capture the perimeter contribution to DCR, a 2D modeling of the SPAD is also required. In this paper, a TCAD-based simulation environment capable of simulating 2D DCR characteristics of Si SPADs is developed by proposing two methods of calculating the DCR. Several test-structures with different perimeter termination of the Si p^+n diode regions are proposed to compare and assess the applicability of the methods. The developed environment is used to calculate the total DCR of the PureB SPADs, showing excellent agreement with the measurements. Using the proposed simulation environment PureB SPADs with an implicit guard ring (GR) are examined. The sources of DCR are identified and the critical regions are located. The optimization of the fabrication parameters to reduce the DCR in PureB SPADs is considered and briefly discussed.

2. DARK COUNT RATE MODELLING IN A TCAD ENVIRONMENT

2.1 1D theoretical treatment

Theoretical treatment for modeling of 1D SPAD behavior is first given. The probabilities that an electron or a hole can start an avalanche (P_e, P_h) are derived in the 1D case by Oldham et al.[23]. The probabilities that an electron or a hole injected into the high-field region from any position in the structure (x) will cause an avalanche are calculated as:

$$\frac{dP_e}{dx} = (1 - P_e) \cdot \alpha_e (P_e + P_h - P_e P_h), \tag{1}$$

$$\frac{dP_h}{dx} = -(1 - P_h) \cdot \alpha_h (P_e + P_h - P_e P_h), \tag{2}$$

where α_e and α_h are impact ionization coefficients for electrons and holes, respectively. The differential equations are solved with boundary conditions for *pn*-junction diode of $P_e(x_{start}) = 0$ and $P_h(x_{end}) = 0$ where x_{start} is the beginning of the depletion region and x_{end} is the end of the depletion region having the width $W = x_{end} - x_{start}$. Coefficients α_e and α_h are extracted from a TCAD simulator at different excess bias voltages. Sentaurus Device[20] allows simulations of *I-V* characteristics beyond the breakdown voltage where the impact ionization generation is not included self-consistently into solving the continuity equations. This effectively allows turning off the impact ionization while at the same time the ionization coefficients are calculated for a given structure at a certain V_{EX}.

DCR and PDE are determined using the pair avalanche probability[23]:

$$P_p = P_e + P_h - P_e P_h, \tag{3}$$

and carrier generation rate profiles that can be obtained from the TCAD simulator. In the general form, DCR can be calculated using the equation based on[22]:

$$DCR = \int_W P_p(x) G_{dark}(x)\, dx, \tag{4}$$

where G_{dark} is one of the generation rate profiles caused by the dark carrier generation mechanisms such as SRH, BTBT or TAT. Similarly, the PDE is calculated based on[22] using the optical generation rate profile (G_{photo}) as:

$$OCR = \int_W P_p(x) G_{photo}(x)\, dx, \tag{5}$$

$$PDE = \frac{OCR}{\Phi}, \tag{6}$$

where Φ is the impinging photon flux.

2.2 2D DCR calculation

In a 2D simulation, the ionization coefficients can be extracted at different 1D cross-sections. By placing 1D cross-sections, complete 2D profiles of P_e and P_h can be obtained. In this work, two methods of constructing the 1D cross-sections are proposed: in the "quasi-2D" (Q-2D) method where only vertical 1D cross-sections are assumed, and in the "ionization-integral 2D" (II-2D) method where cross-sections are created at positions where the maximum ionization integrals are calculated as illustrated in Figure 1. The Q-2D method is proposed as a way of simplifying the extraction of the 2D DCR

in a complex structure and if applicable to the geometry of the device the method can be used to analyze 3D DCR without calculation of ionization integrals. First, the study of three test structures employing different GR solutions was performed using the developed 2D calculation methods to analyze the applicability of the developed methods to different geometries.

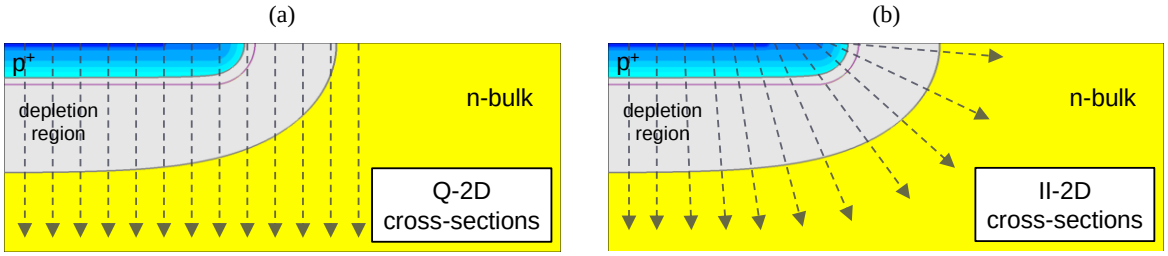

Figure 1. Methods for constructing the 1D cross-sections for 2D avalanche probability calculations: a) "quasi-2D", Q-2D and b) "impact-ionization", II-2D.

To compare the Q-2D and II-2D methods, three Si p^+n diodes test case structures were proposed and analyzed. These are the structures without a guard ring (GR), with an implicit GR, and with a "conventional" lowly-doped GR. The cross-sections of the simulated structures are shown in Figure 2. The simulated doping profile of the active part of the structure is depicted in Figure 3 (a). The p^+ doping profile is a Gaussian with peak concentration (N_{Mp+}) at the surface of 2×10^{19} cm^{-3} and a pn junction depth (y_{jp+}) of 100 nm, defined at a background concentration of 10^{15} cm^{-3}. This low background bulk doping is defined to a depth of 10 μm where a highly doped n^+ region with a concentration of 10^{18} cm^{-3} is placed to prevent full depletion of the substrate as indicated in Figure 3 (a). The multiplication region is located at y_M = 250 nm from the surface with a peak concentration of 2.5×10^{17} cm^{-3} and a diffusion length (D_L) of 75 nm. The breakdown voltage of the active part of the device (V_{BR}) was 32.8 V obtained from 1D simulations and is shown in Figure 3 (b). Avalanche generation was modeled using impact-ionization coefficients as measured by van Overstraeten and de Man[24]. BTBT was simulated using nonlocal tunneling models with default parameters from Sentaurus Device[20] while SRH is simulated with the same electron and hole recombination lifetimes of 100 μs and the position of the trap assumed at the middle of the bandgap.

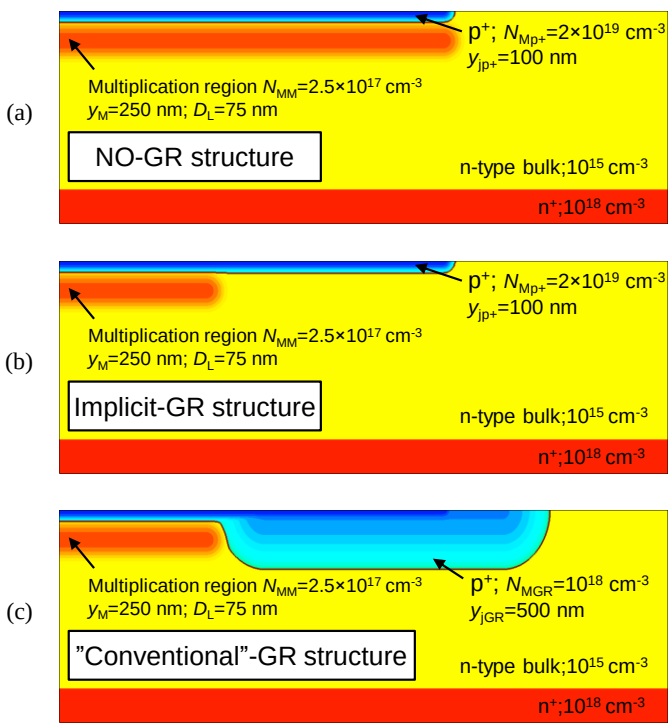

Figure 2. Test case structures used to validate the applicability of the Q-2D and II-2D methods: a) NO-GR structure, b) implicit-GR structure, c) "conventional"-GR structure.

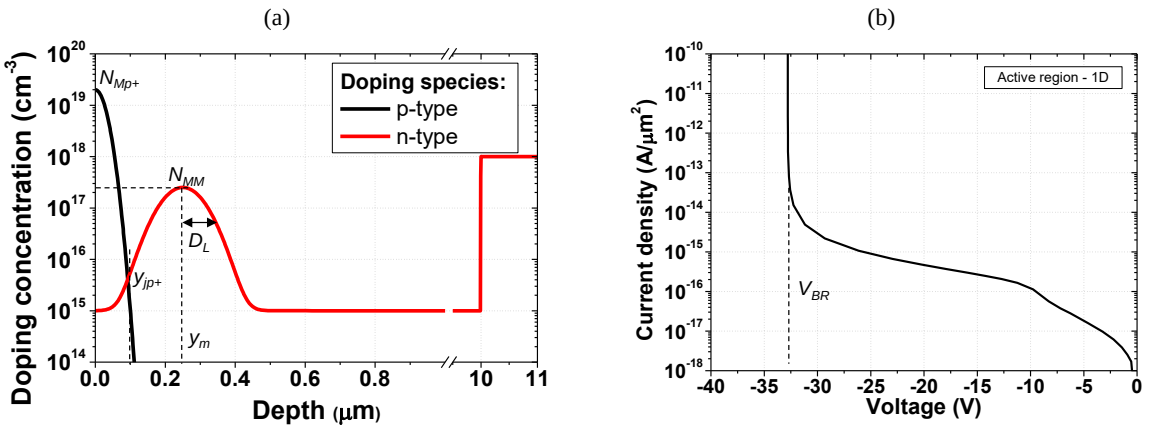

Figure 3. Doping profiles of the simulated active region. (b) *I-V* characteristics of the active region of a device indicating the breakdown voltage.

Impact ionization coefficients for electrons and holes with respect to depth of the simulated 1D structure are shown in Figure 4 (a) at V_{EX} = 1 V, 5 V and 10 V. Using equations (1) and (2) the avalanche probabilities were calculated and are shown in Figure 4 (b) for the same excess bias voltages. SRH and BTBT generation rates with respect to depth are shown in Figure 4 (c). The shape of the SRH profile is determined by the BTBT generation rate which increases the concentration of carriers. From the avalanche probabilities and the generation rates for SRH and BTBT one can calculate the DCR contributions using the equation (4) at each excess bias voltage. This was performed at various V_{EX} voltages and 1D DCR contributions from SRH and BTBT in the active region are plotted in Figure 5. In the active region at V_{EX} = 5 V, the DCR from SRH is 38.8 Hz/μm^2 which is more than three orders of magnitude higher than the BTBT equal to 0.016 Hz/μm^2.

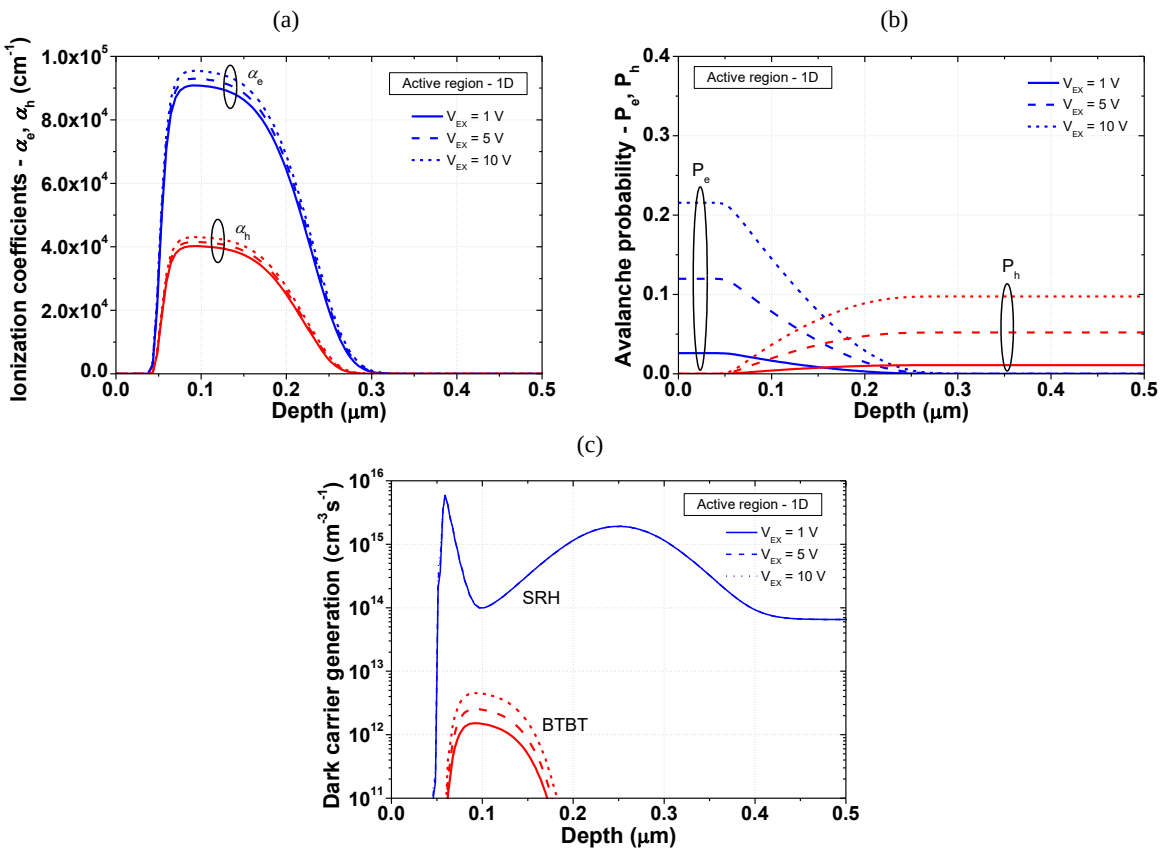

Figure 4. (a) Ionization coefficients for electrons and holes with respect to the depth of the simulated 1D active region. (b) Calculated avalanche probabilities for electrons and holes with respect to the depth of the simulated 1D active region. (c) Generation rates for SRH and BTBT with respect to the depth of the simulated 1D active region.

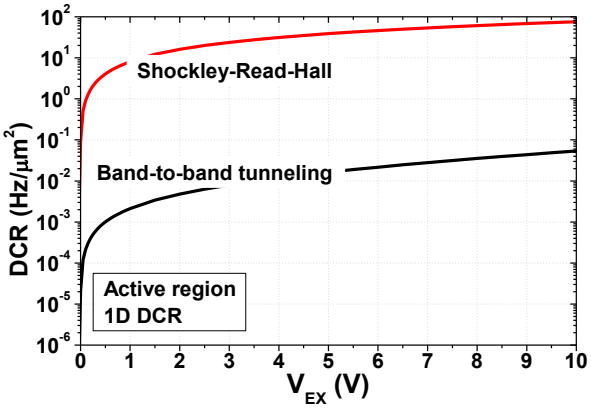

Figure 5. Simulated 1D DCR with respect to V_{EX} in the active region of the test case structures.

The two methods for calculating 2D DCR are compared and the results are given in Table 1. For a given V_{EX} up to 10 V, the NO-GR structure consistently has lower Q-2D than II-2D values. The cause was identified by comparing the plot of the pair avalanche probability calculated using (3) in the depletion region of the two structures at V_{EX} = 5 V. Results are plotted in Figure 6. With the Q-2D method, P_p drops to zero at the depletion periphery because the electric field and associated ionization coefficients are too low along the vertical cross-sections there. The II-2D method gives an appropriate representation of the electric field and P_p is calculated in the whole peripheral depletion region. P_p in the active region is the same for both methods. In contrast, for BTBT generation the critical position is located close to the high-field position where avalanche generation occurs so the integrated DCR calculated by the two methods is practically the same. The implicit-GR structure at V_{EX} = 1 V has the same values of SRH and BTBT DCR since the breakdown is located in the active region. However, with the given abrupt p^+ doping profile, the $V_{BR,per}$ is as low as 37.9 V so for V_{EX} > 5 V the BTBT DCR from this region dominates the total DCR at a V_{EX} of 5 and 10 V where there also is a large increase in integrated DCR values (Table 1). For the "conventional"-GR structure the integrated DCR has the same values for both the Q-2D and II-2D methods because the chosen GR has a low gradient doping profile that ensures that $V_{BR,per} > V_{BR} + V_{EX}$ for all the simulated V_{EX}. The integrated 2D DCR calculated by the II-2D method with respect to V_{EX} is shown in Figure 7 for the implicit and "conventional" GR structures. An increase of the DCR due to the formation of another breakdown region is clearly visible for V_{EX} > 3 V for the structure with an implicit GR.

Table 1. Comparison of integrated 2D-DCR sources of SRH and BTBT, obtained by II-2D and Q-2D cross-section methods.

Structure	**DCR source**	**Method**	**DCR (Hz/μm²) @ V_{EX}**		
			1 V	**5 V**	**10 V**
NO-GR	SRH	II-2D	$7.62\cdot10^{2}$	$1.28\cdot10^{3}$	$1.89\cdot10^{3}$
		Q-2D	$4.64\cdot10^{2}$	$8.92\cdot10^{2}$	$1.39\cdot10^{3}$
	BTBT	II-2D	$1.18\cdot10^{7}$	$5.42\cdot10^{7}$	$2.68\cdot10^{8}$
		Q-2D	$1.36\cdot10^{7}$	$5.91\cdot10^{7}$	$2.81\cdot10^{8}$
Implicit-GR	SRH	II-2D	$4.52\cdot10^{1}$	$3.17\cdot10^{2}$	$7.7\cdot10^{2}$
		Q-2D	$4.52\cdot10^{1}$	$3.09\cdot10^{2}$	$6.58\cdot10^{2}$
	BTBT	II-2D	$1.17\cdot10^{-2}$	$3.66\cdot10^{1}$	$3.05\cdot10^{3}$
		Q-2D	$1.17\cdot10^{-2}$	$7.70\cdot10^{1}$	$3.51\cdot10^{3}$
"Conventional"-GR	SRH	II-2D	$3.39\cdot10^{1}$	$2.59\cdot10^{2}$	$5.09\cdot10^{2}$
		Q-2D	$3.39\cdot10^{1}$	$2.59\cdot10^{2}$	$5.09\cdot10^{2}$
	BTBT	II-2D	$8.69\cdot10^{-3}$	$1.01\cdot10^{-1}$	$2.96\cdot10^{-1}$
		Q-2D	$8.69\cdot10^{-3}$	$1.01\cdot10^{-1}$	$2.96\cdot10^{-1}$

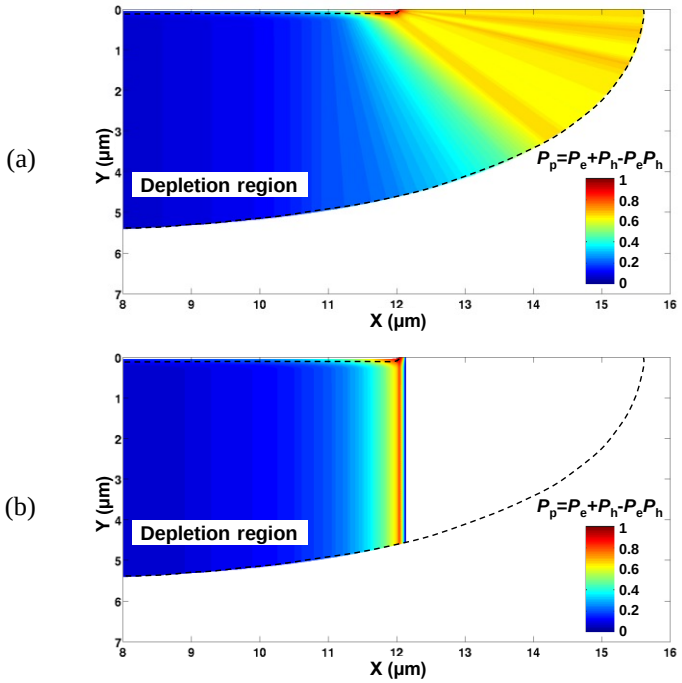

Figure 6. 2D pair avalanche probability of the NO-GR structure at V_{EX} = 5 V derived for a) II-2D and b) Q-2D cross-section methods.

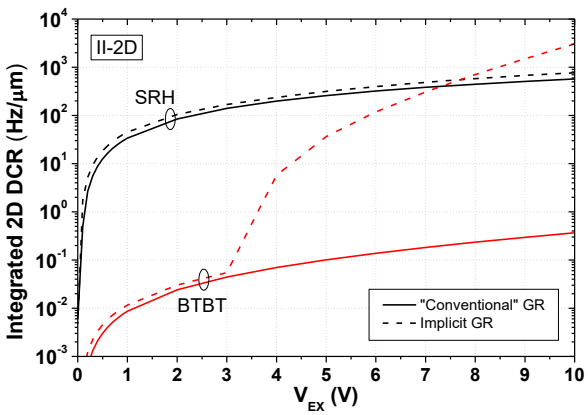

Figure 7. Integrated DCR calculated using the II-2D method with respect to V_{EX} for the structures with implicit and "conventional" GR configurations.

In general, GRs ensure that the peripheral breakdown $V_{BR,per}$ is higher than V_{BR}. An implicit GR is commonly chosen to achieve a compact device and high fill factor in photodetector arrays. Like other GRs they are designed to lower the doping gradient, and thus also the potential gradient, over the corners of the anode perimeter where otherwise the highest electric field and lowest breakdown voltage would be. Moving the breakdown away from the perimeter also has the advantage of avoiding a high field at the SiO_2 interface that otherwise is a source of defect-induced carrier generation. The presented DCR simulation methods are useful for optimizing the compromise between fill factor and the p- and n-doping profiles of the GRs in SPAD devices like the experimentally investigated PureB SPADs addressed in the next subsection. The Q-2D method is a way of approximating the avalanche probabilities that gives satisfactory results in structures where the peripheral regions have a small contribution to the DCR, such as can be achieved with conventional GRs. Otherwise, the more precise II-2D method should be employed. The Q-2D method can provide a way of assessing the DCR contribution in a 3D device by simulating only a portion of the device without performing computationally expensive 3D simulations. This can shorten the process of optimizing the final structure of the device when the SPAD-enabled TCAD simulation environment, presented here, can be utilized.

3. ANALYSIS OF FABRICATED PUREB SPADS USING THE DEVELOPED TCAD ENVIRONMENT

3.1 Process simulations of PureB SPAD fabrication steps

Process simulations using Sentaurus Process[25] were performed following the fabrication steps for the PureB SPADs characterized in [26]. A schematic cross section of the PureB SPAD is shown in Figure 8 (a). The buried layer was simulated with constant phosphorus doping concentration of 10^{18} cm^{-3}. The epitaxial region with a thickness t_{epi} = 1 µm and phosphorus doping concentration $N_{epi} = 10^{15}$ cm^{-3} was deposited on top of the n$^+$ buried layer. The implicit GR was formed by a phosphorus implanted n-enrichment region through a 30-nm-thick thermal oxide into the epi-layer. It is a 2-step implantation composed of first 10^{12} cm^{-2} (Q_{e1}) at 40 keV (E_{e1}) and then 5×10^{12} cm^{-2} (Q_{e2}) at 300 keV (E_{e2}), annealed at 950 °C for 20 min. In the simulations, the PureB anode was approximated by a diffusion into the n-Si from an unlimited source of boron. The PureB deposition was performed for 6 min at 700 °C followed *in-situ* by a 2.5-nm-thick Si deposition doped with boron to a concentration of 10^{18} cm^{-3} and a final anneal at 850 °C for 1 min. This sets the maximum B-doping concentration at 6×10^{19} cm^{-3}. The final simulated doping profiles are shown in Figure 8 (b).

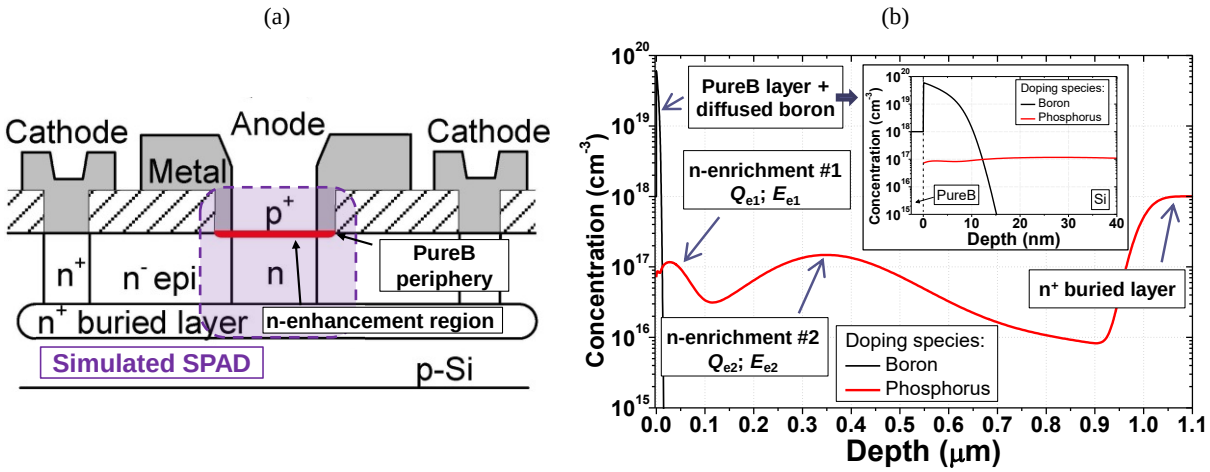

Figure 8. (a) Cross section of a PureB SPAD indicating the simulated region. (b) Doping concentration profile after all the simulated processing steps. Inset: Close-up of the doping concentration profile near the interface indicating the pn-junction depth.

3.2 DCR contributions in PureB SPADs

Device simulations were performed both in 1D and 2D in Sentaurus Device[20] using the structure obtained from the process simulations. Avalanche generation was modeled using impact-ionization coefficients from the University of Bologna impact-ionization model[26]. When applied in the simulations, TAT and BTBT were both simulated using nonlocal tunneling models[20]. Thermal generation was modeled using the SRH model, the parameters of which were fitted to achieve the low saturation current density characteristics typical of PureB photodiodes[12,27]. Electron and hole lifetimes in the SRH model equal 2×10^{-5} s while the position of the trap was 0.15 eV from the middle of the bandgap towards the conduction band. BTBT was simulated using the nonlocal Sentaurus Device model for which the generation term, G_{BTBT}, can be reduced to Kane's model in the uniform electric field limit[28]:

$$G_{BTBT} = AF^{C} exp\left(-\frac{B}{F}\right), \quad (7)$$

where F is the electric field, A and B are coefficients of the model, C is the coefficient which equals 2 for the direct tunneling process, and 2.5 for the phonon-assisted tunneling process. The parameters of the model used in the simulations are $A = 1\times10^{14}$ cm^{-3} s^{-1} and $B = 2.7\times10^{7}$ V/cm which lie in the theoretical range between 1.9×10^{7} V/cm [29] and 3.1×10^{7} V/cm [30]. The parameters used for the traps placed at the anode periphery and applied in the TAT model had a trap concentration of 10^{11} cm^{-3}, a cross section of 10^{-15} cm^2 and the position of the trap was 0.3 eV from the middle of the bandgap towards conduction band. The V_{BR} of the device obtained using the default processing parameters equals 14 V [13] while the simulations of only the n-enhancement part of the device resulted in a V_{BR} of 13.7 V.

A comparison was made to measurements of the PureB SPADs[13] that have a room temperature DCR as low as 5 Hz at V_{EX} = 0.5 V. Simulations were performed in a cylindrical coordinate system to obtain 3D generation rate profiles. Only half of the device was simulated and the left edge of the structure was used as an axis of rotation. The DCR generation at certain radial positions in the device were obtained and integrated using the developed II-2D method. The PureB SPAD devices had an implicit GR, a very abrupt 12-nm-deep p^+ region and an n^+ region at a distance of 0.9 µm. Therefore, a low perimeter breakdown voltage with high DCR was predicted by the simulations at V_{EX} = 5 V as shown in Figure 9. The presence of two DCR sources is clearly visible – one is located at the active part of the device, while the second one is at the PureB periphery.

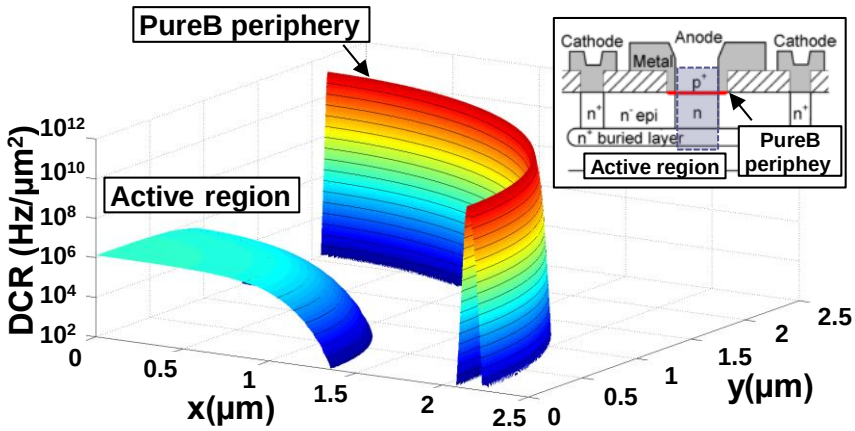

Figure 9. 3D BTBT DCR distribution in PureB SPAD simulated at V_{EX} = 5 V.

In addition to SRH and BTBT generation, trap-assisted tunneling (TAT) generation was also simulated to account for defects at the oxide termination of the p^+-n junction perimeter. As shown in Figure 10, excellent agreement with measurements was obtained. The SRH, TAT and BTBT with the used model coefficients all contribute to the total DCR, but the TAT and BTBT impact starts at $V_{EX} \approx 3.5$ V due to the high electric field at the periphery. Due to the oxide termination of the p^+-n junction perimeter, TAT there plays the dominate role in the DCR when the perimeter breakdown has been reached. For a higher excess voltage, the electric field becomes higher and the perimeter BTBT becomes dominant. There are several sources contributing to the DCR and the process non-uniformity can introduce additional DCR sources which are not covered by simulations. From simulations, the DCR contributions at certain positions in the detector could be identified offering a way to optimize the structure and reduce the contributions to the total DCR. In this respect, since the major source of the DCR originates from the field-enhanced sources such as BTBT and TAT, the optimization of the structure should go in the direction of minimizing the electric field at the edge and making the implicit GR more efficient. The optimization would include reducing the doping concentration in the epitaxial region or increasing the thickness of the epitaxial region.

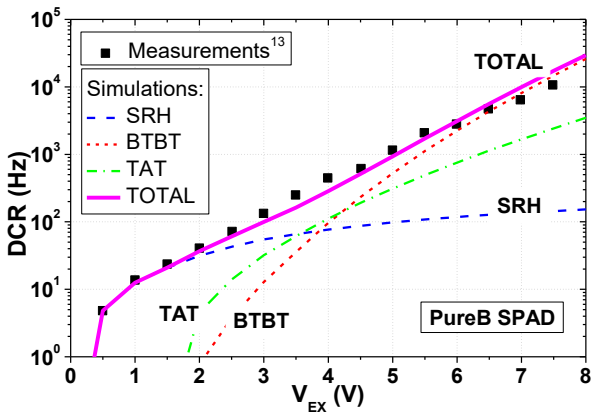

Figure 10. Comparison of the measured and simulated DCR for $Q_{e1} = 1\times10^{12}$ cm^{-2} for the PureB SPAD. The total simulated DCR is comprised of the SRH, TAT and BTBT contributions.

4. CONCLUSIONS

The functionality of the TCAD software was extended to model the discrete events such as DCR by developing a numerical simulation procedure that is able to calculate the avalanche probabilities in 1D. The method was further expanded to also cover the 2D DCR calculations. Two methods of performing the 2D DCR analysis in SPADs were proposed and assessed for validity. The Q-2D method is a way of approximating the avalanche probabilities that gives satisfactory results in structures where the peripheral regions have a small contribution to the DCR, such as can be achieved with conventional GRs. Otherwise, the more precise II-2D method should be employed. The presented DCR simulation methods could be useful for optimizing the compromise between fill factor and the p- and n-doping profiles of the GRs in SPAD devices. The Q-2D method can provide a way of assessing the DCR contribution in a 3D device by simulating only a portion of the device without performing computationally expensive 3D simulations.

The developed simulation method was used to analyze DCR contributions in PureB SPADs. For the experimentally investigated PureB SPADs excellent agreement of the measured and simulated DCR was achieved. Using the assumed SRH, BTBT and TAT parameters, the different contributions to the DCR expose the critical spots in geometry of the device. The very steep PureB p^+n junction with sharp corners at the perimeter, results in high potential gradients that require careful design of the n-doped region to prevent tunneling events from becoming a dominating source of dark counts. A reduction of the DCR contribution coming from the field assisted processes could be achieved by increasing the n-epi-layer thickness or lowering the doping of the epitaxial layer. A high electric field at the vertical pn junction in the active region could also be minimized by modifying the processing parameters of the n-enrichment region implantation. Lowering the donor concentration at the p^+n junction of the n-enhancement region increases breakdown voltage and lowers the BTBT contribution to the DCR. These are precautions that also would lower the capacitance of the SPAD but at the expense of an increased series resistance. Therefore, there is a trade-off between speed and DCR that needs to be considered.

REFERENCES

[1] Hemmati, H., Biswas, A. and Djordjevic, I. B., "Deep-Space Optical Communications: Future Perspectives and Applications," Proceedings of the IEEE 99(11), 2020–2039 (2011).

[2] Shin, D., Xu, F., Venkatraman, D., Lussana, R., Villa, F., Zappa, F., Goyal, V. K., Wong, F. N. C. and Shapiro, J. H., "Photon-efficient imaging with a single-photon camera," Nature Communications 7, 12046 (2016).

[3] Niclass, C., Rochas, A., Besse, P.-A. and Charbon, E., "Design and characterization of a CMOS 3-D image sensor based on single photon avalanche diodes," IEEE Journal of Solid-State Circuits 40(9), 1847–1854 (2005).

[4] Antolovic, I. M., Burri, S., Bruschini, C., Hoebe, R. A. and Charbon, E., "SPAD imagers for super resolution localization microscopy enable analysis of fast fluorophore blinking," Scientific Reports 7, 44108 (2017).

[5] Li, D. D.-U., Ameer-Beg, S., Arlt, J., Tyndall, D., Walker, R., Matthews, D. R., Visitkul, V., Richardson, J. and Henderson, R. K., "Time-Domain Fluorescence Lifetime Imaging Techniques Suitable for Solid-State Imaging Sensor Arrays," Sensors 12(12), 5650–5669 (2012).

[6] Lewellen, T. K., "Recent developments in PET detector technology," Physics in Medicine and Biology 53(17), R287–R317 (2008).

[7] Nielsen, M. A. and Chuang, I. L., "Quantum Computation and Quantum Information: 10th Anniversary Edition" (2011).

[8] Ekert, A. K., "Quantum cryptography based on Bell's theorem," Physical Review Letters 67(6), 661–663 (1991).

[9] Bennett, C. H. and Brassard, G., "Quantum cryptography: Public key distribution and coin tossing," Proc. of the IEEE Int. Conf. on Computers, Systems & Signal Processing, 175–179 (1984).

[10] Shi, L., Nihtianov, S., Xia, S., Nanver, L. K., Gottwald, A. and Scholze, F., "Electrical and Optical Performance Investigation of Si-Based Ultrashallow-Junction p+-n VUV/EUV Photodiodes," IEEE Transactions on Instrumentation and Measurement 61(5), 1268–1277 (2012).

[11] Šakić, A., Nanver, L. K., Van Veen, G., Kooijman, K., Vogelsang, P., Scholtes, T. L. M., De Boer, W., Wien, W. H. A., Milosavljević, S., Heerkens, C. T. H. and others., "Versatile silicon photodiode detector technology for scanning electron microscopy with high-efficiency sub-5 keV electron detection," Electron Devices Meeting (IEDM), 2010 IEEE International, 31–4, IEEE (2010).

[12] Nanver, L. K., Qi, L., Mohammadi, V., Mok, K. R. M., de Boer, W. B., Golshani, N., Sammak, A., Scholtes, T. L. M., Gottwald, A., Kroth, U. and Scholze, F., "Robust UV/VUV/EUV PureB Photodiode Detector Technology With High CMOS Compatibility," IEEE Journal of Selected Topics in Quantum Electronics 20(6), 306–316 (2014).
[13] Qi, L., Mok, K. R. C., Aminian, M., Charbon, E. and Nanver, L. K., "UV-Sensitive Low Dark-Count PureB Single-Photon Avalanche Diode," IEEE Transactions on Electron Devices 61(11), 3768–3774 (2014).
[14] Qi, L., Sluyterman, S., Kooijman, K., Mok, K. R. C. and Nanver, L. K., "PureB single-photon avalanche diodes for low-energy electron detection down to 200 eV," Optics Letters 40(3), 300 (2015).
[15] Sze, S. M. and Ng, K. K., [Physics of Semiconductor Devices, 3rd edition], Wiley-Interscience, Hoboken, N.J (2006).
[16] Rech, I., Ingargiola, A., Spinelli, R., Labanca, I., Marangoni, S., Ghioni, M. and Cova, S., "Optical crosstalk in single photon avalanche diode arrays: a new complete model," Optics express 16(12), 8381–8394 (2008).
[17] Webster, E. A. G. and Henderson, R. K., "A TCAD and Spectroscopy Study of Dark Count Mechanisms in Single-Photon Avalanche Diodes," IEEE Transactions on Electron Devices 60(12), 4014–4019 (2013).
[18] Cova, S., Lacaita, A. and Ripamonti, G., "Trapping phenomena in avalanche photodiodes on nanosecond scale," IEEE Electron Device Letters 12(12), 685–687 (1991).
[19] Cova, S., Ghioni, M., Lacaita, A., Samori, C. and Zappa, F., "Avalanche photodiodes and quenching circuits for single-photon detection," Applied optics 35(12), 1956–1976 (1996).
[20] Synopsys., [Sentaurus Device User Guide], Synopsys, Mountain View, CA, USA (2016).
[21] Knežević, T. and Suligoj, T., "Examination of the InP/InGaAs single-photon avalanche diodes by establishing a new TCAD-based simulation environment," Simulation of Semiconductor Processes and Devices (SISPAD), 2016 International Conference on, 57–60, IEEE (2016).
[22] Donnelly, J. P., Duerr, E. K., Mcintosh, K. A., Dauler, E. A., Oakley, D. C., Groves, S. H., Vineis, C. J., Mahoney, L. J., Molvar, K. M., Hopman, P. I., Jensen, K. E., Smith, G. M., Verghese, S. and Shaver, D. C., "Design Considerations for 1.06-um InGaAsP–InP Geiger-Mode Avalanche Photodiodes," IEEE Journal of Quantum Electronics 42(8), 797–809 (2006).
[23] Oldham, W. G., Samuelson, R. R. and Antognetti, P., "Triggering phenomena in avalanche diodes," IEEE Transactions on electron devices 19(9), 1056–1060 (1972).
[24] Van Overstraeten, R. and De Man, H., "Measurement of the ionization rates in diffused silicon p-n junctions," Solid-State Electronics 13(5), 583–608 (1970).
[25] Synopsys., [Sentaurus Process User Guide], Synopsys, Mountain View, CA, USA (2016).
[26] Vecchi, M. C. and Rudan, M., "Modeling electron and hole transport with full-band structure effects by means of the spherical-harmonics expansion of the BTE," IEEE Transactions on Electron Devices 45(1), 230–238 (1998).
[27] Sarubbi, F., Nanver, L. K. and Scholtes, T. L. M., "High Effective Gummel Number of CVD Boron Layers in Ultrashallow p+n Diode Configurations," IEEE Transactions on Electron Devices 57(6), 1269–1278 (2010).
[28] Kane, E. O., "Theory of Tunneling," Journal of Applied Physics 32(1), 83 (1961).
[29] Hurkx, G. A. M., "On the modelling of tunnelling currents in reverse-biased p-n junctions," Solid-State Electronics 32(8), 665–668 (1989).
[30] Logan, R. A. and Chynoweth, A. G., "Effect of degenerate semiconductor band structure on current-voltage characteristics of silicon tunnel diodes," Physical Review 131(1), 89 (1963).